JACS
JOURNAL OF THE AMERICAN CHEMICAL SOCIETY
pubs.acs.org/JACS
Article

Open Access
This article is licensed under CC-BY-NC-ND 4.0

# pH-Driven Restructuring of Hydration Layers and Cation Adsorption at the Alumina−Water Interface

Julia Neumann,* YoungJae Kim, Xiaoyu Wang, Katherine J. Harmon, Amanda J. Carr, Johannes Lützenkirchen, Paul Fenter, and Sang Soo Lee*

Cite This: *J. Am. Chem. Soc.* 2026, 148, 20399−20411

Read Online

ACCESS | Metrics & More | Article Recommendations | Supporting Information

**ABSTRACT:** Oxide−water interfaces underpin ion separations, catalysis, and electrochemical energy technologies, where the electrical double layer (EDL) controls adsorption, transport, and reactivity. However, the molecular-scale links between pH-dependent surface protonation, hydration-layer structure, and counterion adsorption remain poorly defined. Here, we combine in situ crystal truncation rod (CTR) and resonant anomalous X-ray reflectivity (RAXR) with streaming potential measurements and ab initio molecular dynamics (AIMD) simulations to resolve the chemical and structural evolution of the EDL at the single-crystal alumina (012)−water interface in 10 mM $Rb^+$ over pH 3−12. CTR measurements reveal two distinct adsorbed water layers at ∼2.2 and ∼3.5 Å above the surface. Each water layer shifts toward the substrate at transition pHs near 6.5 and 10.6, respectively, reflecting changes in primary hydration layer structure in response to the deprotonation of bridging and terminal aluminol groups. RAXR shows a 10-fold increase in $Rb^+$ coverage and a decrease in mean adsorption height from ∼3.5 to ∼2.7 Å with increasing pH, indicating enhanced counterion binding accompanied by Stern layer contraction. Streaming potential measurements demonstrate that the zeta potential, i.e., the potential at the hydrodynamic shear plane, is positive at pH 3 and becomes negative at pH ≥ 3.5. The negative charge magnitude increases with increasing pH, consistent with progressive surface deprotonation at higher pH. AIMD identifies inner- and outer-sphere $Rb^+$ complexes whose adsorption heights and coordination geometries depend sensitively on the protonation state of surface oxygens, providing atomistic support for the experimentally inferred trends. These measurements establish two discrete, site-specific pH transitions in hydration-layer structure that track aluminol (de)protonation and quantitatively link them to a pH-driven contraction of the Stern layer (increasing $Rb^+$ coverage and decreasing adsorption height). This provides a direct structural basis for connecting surface acid−base chemistry to ion binding distances at an oxide−water interface.

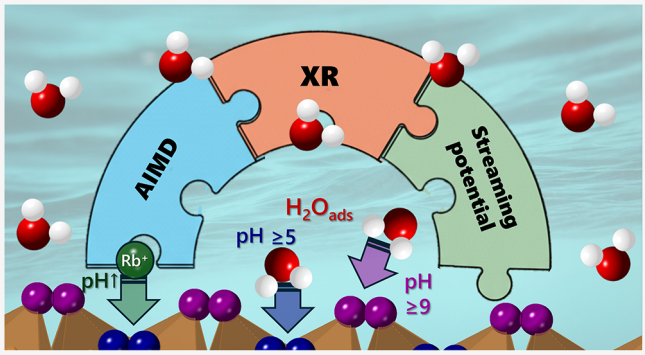


## ■ INTRODUCTION

Metal oxide−water interfaces mediate key physicochemical processes, including ion sequestration, corrosion, heterogeneous catalysis, and electrochemical reactions.[1,2] A molecular-level understanding of their interfacial structure is essential for predictive models of oxide reactivity in environmental and technological settings, and for establishing design principles to tune adsorption, selectivity, and charge transfer.

Among metal oxides, alumina ($\alpha$-$Al_2O_3$) is a widely used model for oxide−water interfaces. Its surfaces expose Al−O(H) functional groups (aluminol groups) that control ion transport and adsorption.[3] These aluminol groups are structurally similar to those of Al-bearing hydroxides and clay minerals, making them a proxy for understanding a broad class of mineral−water interfaces.[1,2,4−6] Alumina has a trigonal crystal structure consisting of a nearly hexagonal close-packed oxygen sublattice, with two-thirds of the octahedral sites occupied by Al. The hydration structure at alumina−water interfaces depends strongly on the type, density, and acidity of the functional groups on various alumina surface orientations.[7−10]

The alumina (01$\bar{1}$2) surface, also referred to as the r-cut or (012) surface (Figure S1 of the Supporting Information), has been extensively studied because its structure resembles that of clay particle edges.[2,6] It is terminated by triply and singly coordinated aluminol groups that undergo acid−base reactions[11,12]

**Received:** December 3, 2025
**Revised:** April 4, 2026
**Accepted:** April 8, 2026
**Published:** May 12, 2026

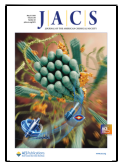

Downloaded from pubs.acs.org/jacsat/article-pdf/148/20/20399/66197993/jacs.5c21453.pdf by guest on 16 October 2026

ACS Publications
© 2026 UChicago Argonne, LLC., Operators of Argonne National Laboratory. Published by American Chemical Society

**Scheme 1. Overview of the Approach to Resolve the pH-Dependent Electrical Double Layer at the Alumina (012)−water Interface**[a]

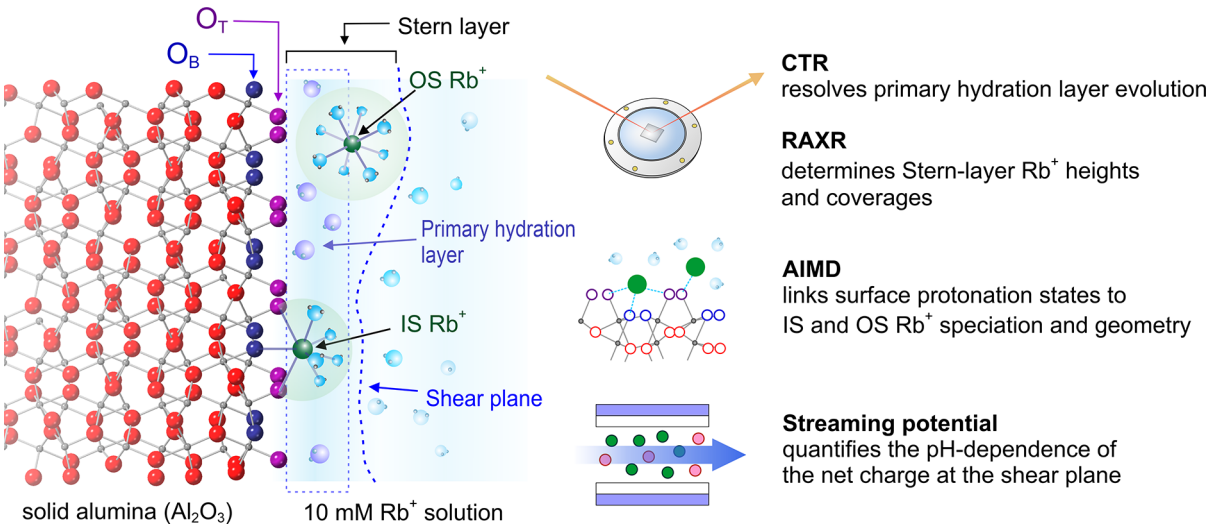


[a]A self-consistent, multiscale picture of EDL evolution that connects atomic-scale structure to macroscopic electrokinetics is explored through the integration of interface-specific X-ray scattering (CTR and RAXR), ab initio molecular dynamics (AIMD), and streaming-potential measurements.

$$>Al_3OH^{0.5+} \rightarrow >Al_3O^{0.5-} + H^+, \qquad pK_a \approx 5 - 6 \tag{1}$$

$$>AlOH_2^{0.5+} \rightarrow >AlOH^{0.5-} + H^+, \qquad pK_a \approx 9 - 11 \tag{2}$$

where $K_a$ is the acid dissociation constant and $pK_a$ is defined as $-\log_{10} K_a$. The oxygen atoms in the $>Al_3O$ and $>AlO$ functional groups are hereafter referred to as bridging and terminal oxygens, i.e., $O_B$ and $O_T$, respectively. (De)-protonation reactions of these functional groups modulate the net surface charge as a function of pH, thereby influencing both the structure of interfacial water and the electrostatic interaction with aqueous ions.[11−15] The point of zero net proton charge (PZNPC)—the pH value at which the net electrical charge on the surface is zero—depends on the type, number density, and protonated state of surface functional groups. Reported "zero-charge" pH values for alumina are inconsistent across the literature.[11,13−17] This is partially because the PZNPC is frequently conflated with the isoelectric point (IEP), despite differing definitions and because of genuine variability in surface chemistry, crystallographic planes, defect densities, and the sensitivity of experimental techniques (see Supporting Information Text S3 and Figure S2 for details). These discrepancies underscore the need to study interfacial processes on well-defined crystalline planes with precisely characterized chemical and structural properties using interface-specific methods.

Several interface-specific experimental techniques have been used to explore the hydration structure at the alumina (012)−water interface. In situ specular crystal truncation rod (CTR) studies[6,9,10] have demonstrated strong positional ordering of interfacial water, controlled by the interaction with the two types of surface aluminol groups. The nonlinear optical vibrational sum frequency generation (SFG) spectroscopy[11,18,19] has shown that the alumina (012)−water interface exhibits two distinct OH stretch bands at 3230 $cm^{-1}$ and 3490 $cm^{-1}$.[11] The 3490 $cm^{-1}$ band is assigned to surface hydroxyl groups, and analysis of the pH-dependence of this SFG response using a two-$pK_a$ approach yielded values of 4.9 and 9.2. The 3230 $cm^{-1}$ band is assigned to interfacial water molecules, and its amplitude changes sign with pH, indicating a shift in the net orientation of interfacial water dipoles caused by a surface charge reversal.[20] These studies reveal that both surface hydroxyls and interfacial water respond strongly to pH changes but do not yet provide quantitative correlations between the two.

In this work, we establish a quantitative molecular-scale connection between (i) the positions of hydration layers, (ii) the magnitude and distribution of surface charge, and (iii) the structure and coverage of adsorbed ions within the electrical double layer (EDL). We combine synchrotron in situ high-resolution X-ray reflectivity (XR), including CTR and resonant anomalous X-ray reflectivity (RAXR), streaming potential measurements, and ab initio molecular dynamics (AIMD) simulations (Scheme 1) to resolve how pH-dependent changes in surface functional group speciation drive the evolution of interfacial hydration and ion adsorption at the alumina (012)−water interface. XR data were collected from pH 3 to 12 at a nearly constant ionic strength ensured by using electrolyte mixtures of HCl/RbCl/RbOH, referred to as $Rb^+$ solutions hereafter, to maintain a comparable Debye length in the diffuse layer.[21] CTR analysis reveals pH-dependent changes in the heights and organization of adsorbed water layers and colocated adsorbed ions within the Stern layer. RAXR provides element-specific $Rb^+$ distributions and coverages, which we interpret with guidance from AIMD simulations that resolve the geometry and occurrence of inner- and outer-sphere complexes as a function of surface protonation state. Streaming potential measurements quantify the pH-dependence of the zeta potential, i.e., the net charge within the shear/hydrodynamic slipping plane (Scheme 1), and allow us to assess how Stern-layer charge inferred from RAXR relates to the electrokinetic response. Details of solution preparation, single-crystal surface preparation and characterization (Figure S3), X-ray cell configuration (Figure S4), and data analysis, AIMD setup, and streaming potential measurements are provided in the Supporting Information document.


https://doi.org/10.1021/jacs.5c21453
J. Am. Chem. Soc. 2026, 148, 20399−20411

Downloaded from pubs.acs.org/jacsat/article-pdf/148/20/20399/66197993/jacs.5c21453.pdf by guest on 16 October 2026

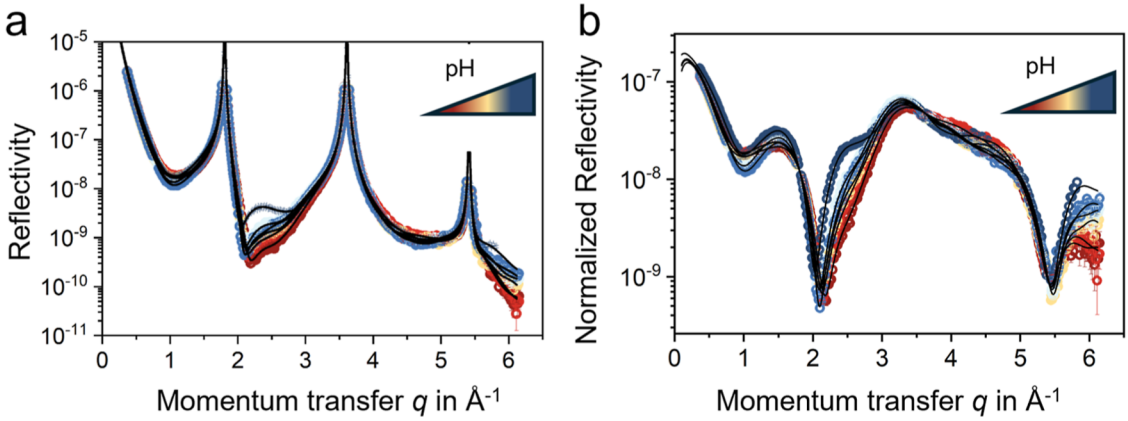


**Figure 1.** Resolving pH-dependent variations in the structure of the alumina (012)−water interface using in situ crystal truncation rod measurements. Original (a) and normalized[35] (b) CTR data for the alumina (012) surface in 10 mM $Rb^+$ solutions at pH 3, 5, 7, 8.5, 10.5, and 12 shown in colored symbols. The CTR curves calculated based on the best-fit models (see Tables S1−S4) for the data sets are displayed as black lines. The CTR plots for individual pH values are shown in Figures S5 and S6.

By integrating these complementary methods, we find that surface deprotonation does not continuously perturb hydration/adsorption but instead produces discrete structural transitions in the primary hydration layers that coincide with distinct aluminol chemistries. This directly constrains how counterions approach the surface as a function of pH, providing experimentally anchored insights for Stern-layer models and surface-complexation descriptions. These results extend prior observations by placing them on a quantitative structural basis and provide benchmarks for developing molecularly informed surface complexation and reactive transport models of oxide−water interfaces.

## ■ RESULTS

### High-Resolution X-ray Reflectivity

Changes in the atomic structure at the alumina (012)−10 mM $Rb^+$ solution interface were investigated using CTR measurements across a pH range of 3−12 (Figures 1a, S5 and S6). The high intensity peaks near $q \approx 1.8$, 3.6, and 5.4 $Å^{-1}$ correspond to the tails of the Bragg reflections of the bulk mineral, i.e., (012), (024), and (036), respectively. Intensity variations in the regions between these peaks are determined by the interfacial structure, including relaxation of surface atoms, changes in surface hydration structure, and adsorption of ions. The CTR patterns after normalization to the generic CTR shape, i.e., $1/[q \sin(qd/2)]^2$, where $d$ is the (012) layer spacing of alumina (≈3.48 Å), are shown in Figures 1b, S5 and S6. By applying this normalization, the contribution of the substrate Bragg peaks is minimized, and subtle variations resulting from the surface structure become more visible. The data clearly show systematic changes with varying solution pH. For example, small oscillations in $0.5 \leq q \leq 1.5$ $Å^{-1}$ become more pronounced with increasing pH. Similar pH-dependent changes are observed in $2 \leq q \leq 3$ $Å^{-1}$.

CTR data analysis yields total electron−density profiles along the surface-normal direction, providing a direct pH-dependent measure of the interfacial structure, including surface relaxations and adsorbed water and ion distributions. The best-fit structural models (Tables S1−S3) show non-monotonic variations in the total electron−density profile at the alumina−water interface across the investigated pH values (Figure 2).

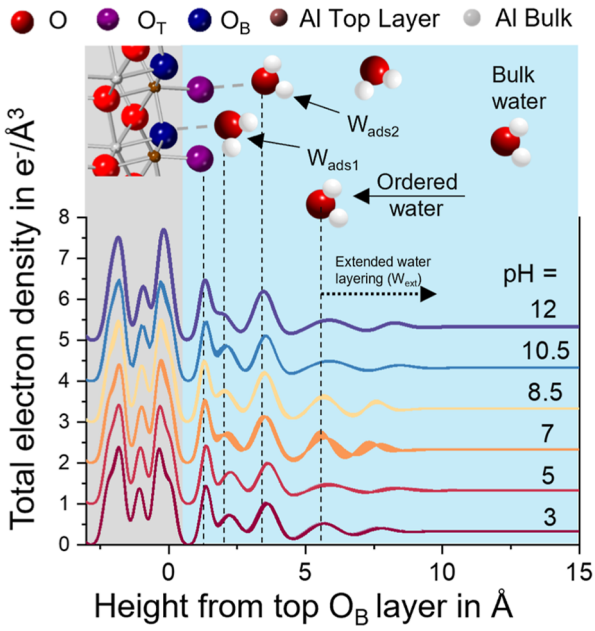


**Figure 2.** Evolution of the hydration structure of the alumina (012)−water interface in 10 mM RbCl/RbOH solution as a function of pH. Total electron-density profiles (solid bands) as a function of height from the crystallographic $O_B$ position ($z$ = 0 Å) at alumina (012). Thickness of the bands corresponds to the differences in electron density between the analysis of duplicate CTR data. The pH 3 profile is displayed without vertical offset, and each subsequent profile is vertically offset by +1 relative to the previous one. The top schematic illustrates water molecules adsorbed onto $O_B$ and $O_T$ and those organized farther from the interface.

The $O_T$ in the >AlO site is located at a height above the crystallographic, unrelaxed $O_B$ layer, $z$, of ∼1.35 Å. Over the pH range, the $O_T$ shows <0.1 Å displacement along the [012] direction from its ideal lattice position (Tables S1−S3). Two adsorbed water layers ($W_{ads1}$ and $W_{ads2}$) are observed at heights of ∼2.2 and ∼3.5 Å, respectively, which are consistent with the heights of the water molecules adsorbed to $O_B$ and $O_T$ reported in previous studies.[9,10] Because CTR data are sensitive to the electron density, these heights reflect those of the oxygen atoms, rather than the hydrogen atoms in the adsorbed water molecules.

Downloaded from pubs.acs.org/jacsat/article-pdf/148/20/20399/66197993/jacs.5c21453.pdf by guest on 16 October 2026


https://doi.org/10.1021/jacs.5c21453
J. Am. Chem. Soc. 2026, 148, 20399−20411

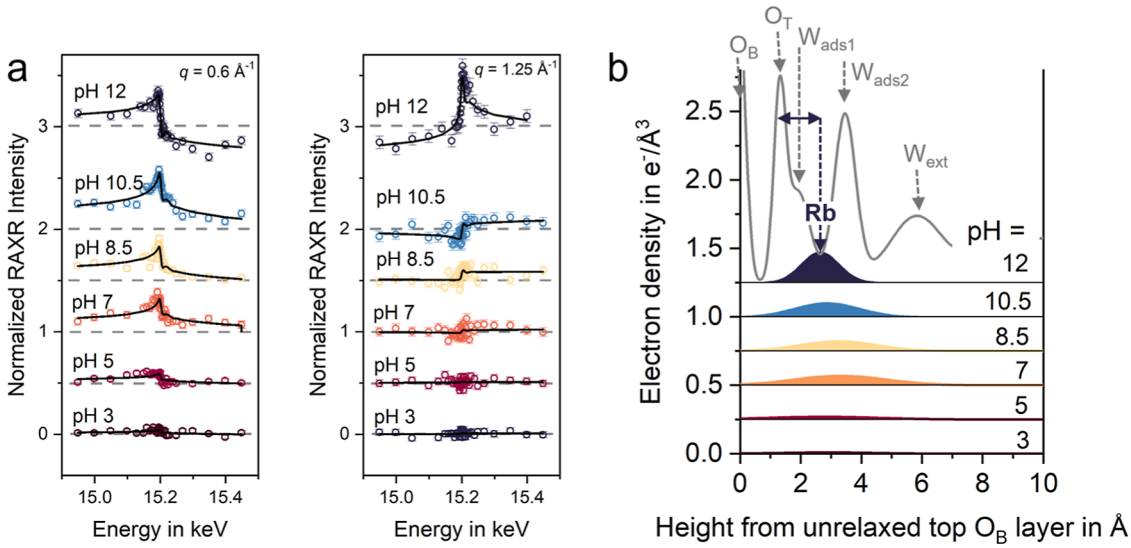


**Figure 3.** pH-dependent changes in the distribution of $Rb^+$ ions adsorbed at the alumina (012)−water interface determined by in situ resonant anomalous X-ray reflectivity. (a). Rb RAXR spectra (symbols) at two selected values of momentum transfer $q$ (left: 0.6 $Å^{-1}$ and right: 1.25 $Å^{-1}$) measured for samples of different pH values. Solid lines are calculated from the best-fit model structures for $Rb^+$ electron density at the interface. Full data sets are shown in Figures S7−S12. Spectra are normalized based on the resonant amplitude normalization method.[36] For clarity, the RAXR spectra at pH 3, 5, 7, 8.5, 10.5, and 12 are vertically offset by +0, 0.5, 1, 1.5, 2, and 3, respectively, as indicated by the gray dashed lines. (b). $Rb^+$ electron-density profiles derived from RAXR data analysis are shown as colored areas with a vertical offset of +0.25 for each pH. For comparison, the total electron-density profile at pH 12 is displayed as a gray solid line in the same units as the Rb-specific density and offset vertically by +1.25.

**Table 1. Best-Fit Parameters Derived from RAXR Data Analysis for the Alumina (012)−10 mM RbCl/RbOH Solution Interface as a Function of Solution pH[a]**

| pH | 3 | 5 | 7 | 8.5 | 10.5 | 12 |
|---|---|---|---|---|---|---|
| $occ_{tot}$ ($Rb^+/A_{UC}$) | 0.024(8) | 0.063(13) | 0.136(14) | 0.146(10) | 0.182(10) | 0.229(12) |
| $occ_{tot}$ ($Rb^+/nm^2$) | 0.097(3) | 0.26(5) | 0.56(6) | 0.60(4) | 0.75(4) | 0.94(5) |
| $\sigma(Rb^+)$ ($C/m^2$) | 0.016(5) | 0.041(8) | 0.089(9) | 0.096(7) | 0.120(7) | 0.151(8) |
| $z_{Rb}$ (Å) | 2.87(23) | 2.76(16) | 3.45(6) | 3.24(5) | 2.86(5) | 2.65(3) |
| $u_{Rb}$ (Å) | 1.52(39) | 1.88(23) | 1.65(12) | 1.19(9) | 1.00(8) | 0.35(15) |
| $\chi^2$ | 0.86 | 1.03 | 1.37 | 1.36 | 1.66 | 2.90 |
| $R$-factor (%) | 1.1 | 1.5 | 1.4 | 1.6 | 1.5 | 1.9 |

[a] $occ_{tot}$: Total $Rb^+$ occupancy in $Rb^+/A_{UC}$ where $A_{UC}$ is calculated as 24.39 $Å^2$ for alumina (012),[22] $\sigma(Rb^+)$: amount of charge compensated by adsorbed $Rb^+$, $z_{Rb}$: adsorption height of $Rb^+$ where $z = 0$ Å is marked by the unrelaxed topmost $O_B$ layer, and $u_{Rb}$: rms distribution width of the adsorbed $Rb^+$ profile. Statistical uncertainties of fit parameters are given in parentheses.

Beyond the first two adsorbed water layers, we identify the presence of extended water layering, $W_{ext}$ (Figure 2), that exhibits pH-dependent broadening and density oscillations. Across the pH range, the first peak in $W_{ext}$ appears at $z \approx 5.7$ Å, followed by oscillations that extend farther from the surface, indicating a broad distribution of water adsorption heights and persistent surface-induced ordering. Among the profiles, those at pH $\leq 5$ or pH $\geq 10.5$ show more gradually varying, lower-amplitude oscillations that farther extend from the surface. In contrast, the profiles at pH 7 and 8.5 show larger amplitude oscillations in the first two $W_{ext}$ layers, but the layering decays over a shorter distance from the surface.

## Resonant Anomalous X-ray Reflectivity

Although the nonmonotonic pH-dependent changes in the total electron−density profile at the alumina (012)−solution interfaces can be explained by rearrangements of the adsorbed water layers, contributions from specifically adsorbed ions must also be considered. Inner-sphere (IS) complexation of $Rb^+$ or $Cl^-$ at surface sites would displace water molecules associated with surface $O_B$ or $O_T$ groups, altering the local hydration structure at the interfaces. Direct ion-specific measurements of interfacial ion distributions are needed to fully interpret the CTR results.

The distribution of $Rb^+$ ions adsorbed at the alumina (012)−water interface was determined using RAXR. The spectra at low pH ($\leq$5) show small but nonzero modulations around the Rb K-edge energy (Figure 3a). The magnitudes of the RAXR signal become larger with increasing pH, reflecting increases in $Rb^+$ coverage.

The RAXR spectra were analyzed using a structural model to determine the total coverage, average adsorption height, and rms-distribution width of $Rb^+$ species adsorbed on the alumina (012) surface (Table 1). We used a Gaussian model to provide a simple description of the ordered $Rb^+$ distributions that are directly comparable over a wide pH range. However, this approach cannot capture the intrinsic complexity of the EDL structure, including distinctions between IS and outer-sphere (OS) species or the presence of a diffuse ion profile. The derived $Rb^+$ coverages at pH 3 and 5 are 0.024 and 0.063 $Rb^+/A_{UC}$, respectively, where $A_{UC}$ is the area of the unit cell and is 24.39 $Å^2$ for alumina (012).[22] The highest $Rb^+$ coverage


https://doi.org/10.1021/jacs.5c21453
J. Am. Chem. Soc. 2026, 148, 20399−20411

Downloaded from pubs.acs.org/jacsat/article-pdf/148/20/20399/66197993/jacs.5c21453.pdf by guest on 16 October 2026

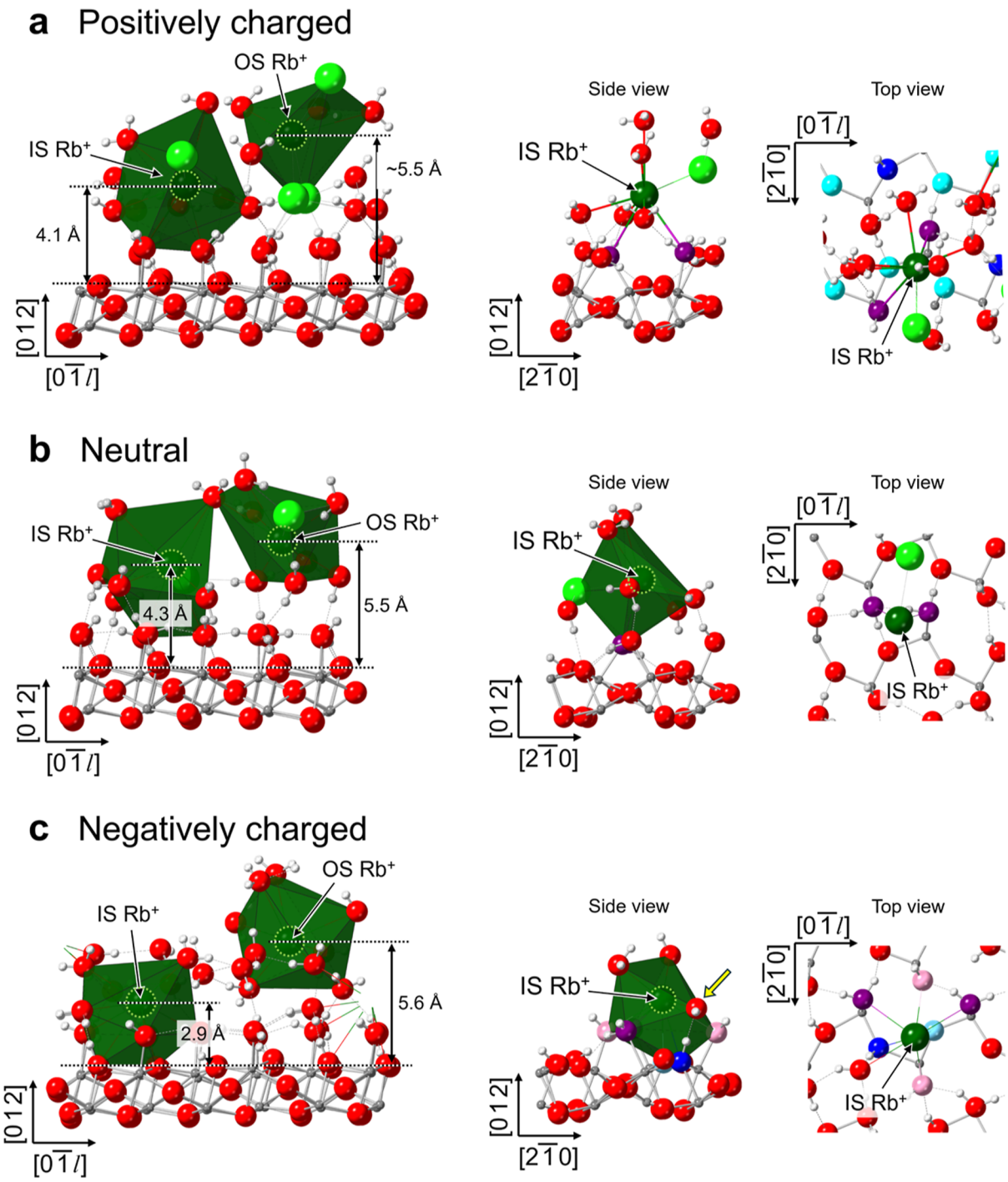


**Figure 4.** Sorption geometries of $Rb^+$ ions adsorbed at the alumina (012)−water interface from ab initio MD simulations. IS and OS $Rb^+$ species adsorbed on positively charged, neutral, and negatively charged alumina surfaces are shown in (a−c), respectively. In left column, the first coordination shells of adsorbed $Rb^+$ ions are depicted as green polyhedra. In each polyhedron, the position of the central $Rb^+$ ion is shown as a dashed circle. Side and top views of IS $Rb^+$ on the surfaces are shown in the middle and right columns, respectively. The $[0\ \bar{1}\ l]$ direction, with noninteger $l \approx 4.96$, is perpendicular to both $[0\ 1\ 2]$ and $[2\ \bar{1}\ 0]$. In the top view, hydrating water molecules are omitted for clarity to highlight the positional relationship between the $Rb^+$ ion and surface oxygen atoms. Color scheme: dark green—$Rb^+$; light green—$Cl^-$; red—O; gray—Al; white—H. In the middle and right columns, the surface oxygen atoms coordinating to IS $Rb^+$ are colored as follows: pink—singly protonated $O_T$; purple—doubly protonated $O_T$; cyan—deprotonated $O_B$; dark blue—singly protonated $O_B$. The $OH^-$ coordinated to IS $Rb^+$ on the negatively charged surface is indicated with a yellow arrow.

measured by RAXR was 0.229 $Rb^+/A_{UC}$ at pH 12. The analysis also shows systematic changes in the adsorbed $Rb^+$ distribution at the alumina−water interface with increasing pH. The adsorption height of $Rb^+$ decreases from 3.5 Å at pH 7 to 2.7 Å at pH 12 (Table 1). At the same time, the $Rb^+$ distribution width becomes narrower at higher pH. Combined, these changes in adsorption height and width result in significant contraction of the adsorbed $Rb^+$ profile with pH. While $Rb^+$ adsorption at pH 7 extends up to 6 Å from $O_B$, it extends to only ∼4.5 Å at pH 12 (Figure 3b).



https://doi.org/10.1021/jacs.5c21453
J. Am. Chem. Soc. 2026, 148, 20399−20411

Downloaded from pubs.acs.org/jacsat/article-pdf/148/20/20399/66197993/jacs.5c21453.pdf by guest on 16 October 2026

## Molecular Dynamics Simulations

We employed AIMD simulations to understand the relationship between site (de)protonation, surface charge magnitude and distribution, and the speciation of $Rb^+$ ions adsorbed on the alumina (012) surface. AIMD explicitly allows bond breaking/forming and thus can capture interfacial proton-transfer (acid/base) events; indeed, we observe $O_T \rightarrow O_B$ proton transfer in some trajectories (see the AIMD Simulations section in Supporting Information Text S1). However, predicting pH-dependent equilibrium surface speciation (surface functional group p$K_a$ values) is beyond the scope of this work.

The simulations were conducted for positively charged, neutral, and negatively charged surfaces (Figure 4), with net surface charge densities of +0.5, 0, and −0.5 site/$A_{UC}$, (+0.33, 0 and −0.33 C/m$^2$). Charge neutrality was maintained by adding (i) 2 $Rb^+$ + 4 $Cl^-$ (positive surface), (ii) 2 $Rb^+$ + 2 $Cl^-$ (neutral), or (iii) 2 $Rb^+$ (negative). Two $Rb^+$ ions were included to test the occurrence of more than one adsorbed species at the interface within the accessible AIMD time window. While adding more $Rb^+$ ions could improve sampling of interfacial $Rb^+$ configurations, it would further increase the effective electrolyte concentration in the finite simulation cell. The effective $Rb^+$ concentration, is ∼1.7 M, or >100-times the 10 mM solutions used in XR. This is a common AIMD limitation that enables charge neutrality and adsorption events on ps−tens-of-ps time scales. We therefore focus on qualitative trends (e.g., IS vs. OS motifs) rather than quantitative agreement.

For the positively charged surface (Figure 4a), the IS adsorbed $Rb^+$ is bidentate to two $>AlOH_2^+$. This species is coordinated to three water molecules adsorbed to neighboring $>AlOH_2^+$ and to two water molecules and one $Cl^-$ farther from the interface. It is laterally displaced from the nearby deprotonated $O_B$ site rather than directly above it, presumably because of electrostatic repulsion from two adjacent positively charged $O_T$ groups. The $Rb^+$ and $Cl^-$ adsorption heights in this configuration are 4.1 and 5.4 Å, respectively. Furthermore, a second $Rb^+$ is adsorbed in an OS configuration through two $Cl^-$ that are attached to $O_T$ sites via hydrogen bonding.

In the neutral case (Figure 4b), the closest adsorbed $Rb^+$ ion to the alumina surface is in a bidentate binuclear IS complex via direct bonds to two doubly protonated $O_T$ atoms. The IS $Rb^+$ ion retains five water molecules in the hydration shell, three of which are additionally bound to $O_T$ sites. Overall, an IS adsorption height of ∼4.3 Å above the $O_B$ plane is observed. The second $Rb^+$ ion adsorbs to the neutral surface in an OS complex that shares three water molecules with $O_T$ groups. This OS $Rb^+$ ion has an additional five water molecules in its primary hydration shell and an adsorption height of ∼5.5 Å.

For the negatively charged surface (Figure 4c), the surface protonation state leads to considerably smaller $Rb^+$ adsorption heights compared to the previous two cases. Here, the IS $Rb^+$ ion adsorbs in a hexadentate "pocket" surrounded by two $O_B$ atoms, one deprotonated and one singly protonated, and four $O_T$ atoms, two singly and two doubly protonated. The average distance between the $Rb^+$ ion and the singly protonated $O_T$ atoms is ∼2.9 Å, similar to the $Rb^+$−O distance of 2.93 Å in the primary hydration shell of $Rb^+$ measured by EXAFS.[23] The IS $Rb^+$ ion is also coordinated with one hydroxide ion and two water molecules. The average height of the $Rb^+$ to the $O_B$ plane determined by the AIMD simulation is ∼2.9 Å. The OS $Rb^+$ ion adsorbed on the surface by sharing two water molecules in its primary hydration shell with two adjacent $O_T$ atoms, one singly and one doubly protonated. The $Rb^+$ species maintains six additional water molecules in its primary hydration shell. The complex has an adsorption height of ∼5.6 Å from the $O_B$ plane.

For the surface systems containing $Cl^-$ ions, we observed the formation of $Rb^+$−$Cl^-$ ion pairs, which likely resulted from the high effective ion concentration of 1.7 M. We treat this pairing primarily as a finite-size/high-concentration effect rather than evidence that contact ion pairs dominate the experimental interface for 10 mM 1:1 electrolyte solution. Although interfaces can locally enhance ion association via altered dielectric response, contact ion pairing in bulk solution is expected to be limited, and the standard assumption of largely dissociated ions remains reasonable. In addition, our interpretation of the CTR and RAXR data does not require abundant RbCl pairing to explain the observed pH-dependent trends in Stern-layer uptake and adsorption height.

## Streaming Potential Measurements

The pH dependence of the zeta potential at the alumina (012)−10 mM $Rb^+$ solution interface was quantified via streaming potential measurements. The zeta potential reported here is as an electrokinetic proxy for the sign and relative magnitude of the net interfacial charge at the hydrodynamic shear plane, reflecting both surface (de)protonation and partial charge compensation by ions in the Stern layer (e.g., $Rb^+$ distributions resolved by RAXR) and the diffuse layer within the shear plane.

To assess reproducibility and potential hysteresis effects, we compared data sets collected using pH titrations in two directions (i.e., low-to-high pH followed by reversal) on the (012) surfaces of alumina crystals. Additional measurements were conducted using alumina (012) crystals from a different source, via (a) instrument-controlled titrations initiated from multiple starting pH values and (b) a fixed-solution protocol with separately prepared 10 mM Rb solutions at individual target pH values (Figure 5).

For all measurements, the zeta potential is positive under the most acidic conditions investigated and becomes increasingly negative with increasing pH. The data show the IEP around pH 3.5. The increasing magnitude of the negative potential with pH is consistent with pH-dependent surface site deprotonation. Although the magnitude of the negative surface charge continues to increase with pH, the corresponding zeta potentials plateau due to charge compensation by cation adsorption in the Stern layer.[12]

While the measured streaming potential data sets demonstrate consistent trends with pH, the individual measurements show quantitative differences. The absolute magnitude of zeta potentials between the samples from two different manufacturers differs at neutral and high pH, indicating measurable sample-to-sample variability. Near circumneutral conditions, the bidirectional titration data show increased variations in measured potential (light blue and dark blue symbols in Figure 5), indicating reduced stability of the electrokinetic response in this pH range. In addition, the data show modest hysteresis at low pH. Possible causes for this hysteresis include slow equilibration of surface protonation/deprotonation, slow adsorption/desorption of counterions, and/or experimental artifacts such as irregular flow patterns or trapped solution in thin fluid layers.

Downloaded from pubs.acs.org/jacsat/article-pdf/148/20/20399/66197993/jacs.5c21453.pdf by guest on 16 October 2026


https://doi.org/10.1021/jacs.5c21453
J. Am. Chem. Soc. 2026, 148, 20399−20411

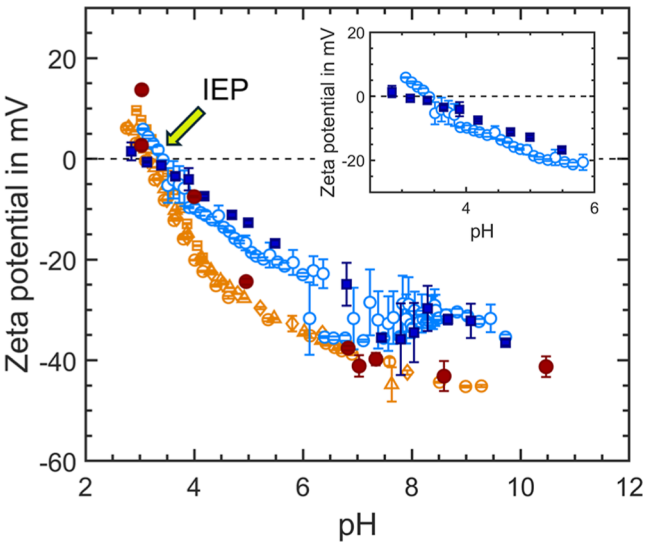


**Figure 5.** Zeta potential measurements of alumina (012)−10 mM RbCl interfaces as a function of pH. The data collected with crystals from the same vendor (MTI Corporation) as that for X-ray measurements are shown in light blue circles for titration from pH 3 to pH 9.7 using 10 mM RbOH and dark blue squares for subsequent reverse titration from pH 9.7 to 2.8 using 50 mM HCl. The inset highlights small differences between these data at pH < 6. Open orange symbols are zeta potentials measured using crystals from a different vendor (SurfaceNet) using the instrument titration system with decreasing pH, starting from four initial pH values—4.2 (squares), 7.6 (triangles), 7.9 (diamonds), and 9.3 (circles)—to pH ∼3. Dark brown circles are data measured with the SurfaceNet crystals using a series of separately prepared 10 mM Rb solutions at target pH values (with rinsing between solutions).

It is important to note that zeta potential reflects the electrostatic potential within the hydrodynamic shear plane rather than the proton-related charge of the mineral surface. For 10 mM 1:1 electrolyte, literature estimates the shear plane located at a distance on the order of ∼30 Å from the charged surface,[12,24] significantly farther than the distribution of Stern-layer $Rb^+$ adsorbed at the alumina−water interface. Accordingly, the persistent negative zeta potential at acidic pH can occur even if the surface remains positively charged. The chemical species causing this negative potential at the shear plane remains speculative; however, we posit that the differences in the location of the hydrodynamic shear plane relative to the Stern layer and oxide surface explain the apparent offset between the PZNPC inferred from SFG (near pH 6.7)[11] and the IEP determined by our streaming potential measurements (∼3.5), reflecting the combined effects of specific adsorption and the distinct sensitivities of electrokinetics versus interface-specific structural probes.

## ■ DISCUSSION

### Response of Adsorbed Water Heights to Site Deprotonation

Effects of pH on the interfacial water structure on alumina (012) are manifested in subtle but systematic changes of the individual species, consistent with findings of a previous study performed in the limited pH range between 5 and 9.[10] Water molecules adsorbed on $O_B$ in the $>Al_3O$ functional group, $W_{ads1}$, show a pronounced pH response, shifting closer to the surface from $z$ of ∼2.2 Å at pH ≤ 5 to ∼2.0 Å at pH > 7 (Figure 6a). Water molecules adsorbed on $O_T$ in the >AlO functional group, $W_{ads2}$, exhibit a similar response at higher pH (>10). Because of this higher onset pH and the limited pH range of our data set, the full transition on this site may not have been captured in the CTR analyses.

We modeled the pH-dependent changes in adsorbed water heights using a simple two-state description to determine transition pH values ($pH_t$) for each site. These $pH_t$ values are analogous to effective $pK_a$ values of the surface functional groups. In this model (see Supporting Information Text S4), the CTR-derived water height from a surface oxygen, $\Delta z = z_W_{ads} - z_O$, is calculated using two end-member heights at extreme pH values, i.e., either pH ≪ $pH_t$ or pH ≫ $pH_t$,

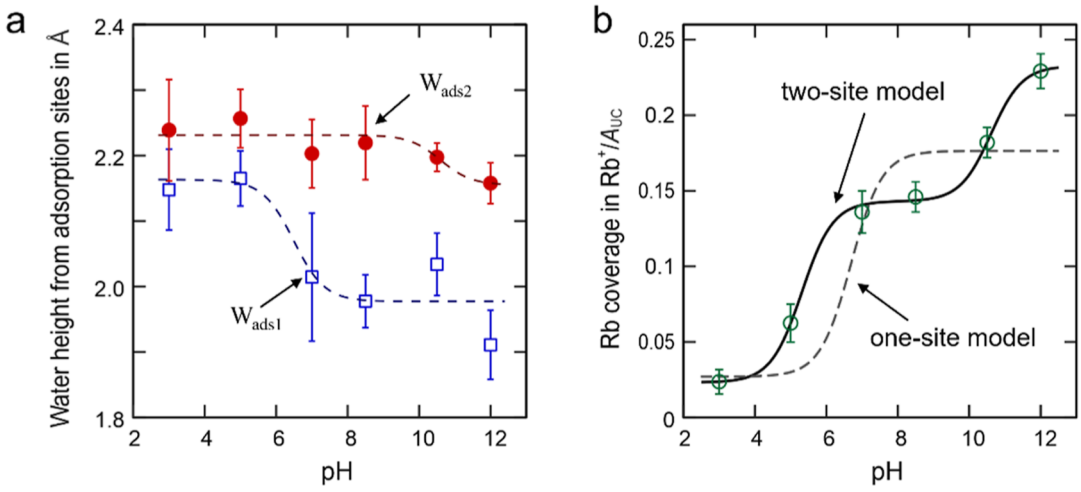


**Figure 6.** pH-dependent response of the interfacial hydration layers and adsorbed $Rb^+$coverage at the alumina (012)−water interface. (a) Heights of the nearest adsorbed water molecules, $W_{ads1}$, measured from the plane of the bridging oxygen, $O_B$, (blue open squares) and the second-nearest adsorbed water molecules, $W_{ads2}$, measured from the plane of terminal oxygen, $O_T$, (red solid circles) as function of pH as obtained from CTR data analysis. The best-fit models to determine the transition pH values are shown as dashed lines (Supporting Information Text S4 and Table 2). (b) Analysis of the pH-dependent variation in adsorbed $Rb^+$ coverage (green open circles) using one-site and two-site models (dashed and solid lines, respectively). See Supporting Information Text S5 and Table 3 for a detailed description of these models.

Downloaded from pubs.acs.org/jacsat/article-pdf/148/20/20399/66197993/jacs.5c21453.pdf by guest on 16 October 2026


https://doi.org/10.1021/jacs.5c21453
J. Am. Chem. Soc. 2026, 148, 20399−20411

respectively. In this relationship, $\Delta z$ remains constant far from $pH_t$ while it varies around the $pH_t$ value with increasing pH.

The optimized model, determined with $\chi^2 = 0.3$ and R-factor = 0.9% (Figure 6a and Table 2), effectively describes the pH-dependent variations in the heights of adsorbed water at the alumina (012)−water interface. The result shows that the height of the $W_{ads1}$ measured from $O_B$ decreases from 2.16 ± 0.04 Å to 1.98 ± 0.03 Å as pH increases around a $pH_{t,1}$ value of 6.5 ± 1.5. Similarly, the height of $W_{ads2}$ measured from $O_T$ decreases from 2.23 ± 0.03 Å to 2.15 ± 0.04 Å around a $pH_{t,2}$ value of 10.6 ± 0.8. The change in the $W_{ads1}$ height is greater than that of $W_{ads2}$, although the latter is likely less accurate because of the limited data at higher pH (Figure 6a). The $pH_t$ values for both sites are also determined with large uncertainties, which is expected given the limited data used for the analysis. In addition, the best-fit model shows an apparent discrepancy for the $W_{ads,1}$ data at the highest pH condition, which may reflect additional structural contributions beyond the assumptions of the two-state model, such as partial overlap of the electron−density profiles of water and adsorbed $Rb^+$ in the near-surface region. Nonetheless, these values align with the theoretical $pK_a$ values of the $>Al_3O$ and $>AlO$ sites[11,12,25] as shown in eqs 1 and 2. To our knowledge, this is the first experimental quantification of systematic, pH-dependent changes in the heights of adsorbed water layers at an oxide−water interface, enabling direct cross-pH comparison of interfacial hydration structure. This work therefore extends and complements prior studies that provided snapshots at fixed pH or across narrow pH ranges.[9,10,26−28]

**Table 2. Best-Fit Model Parameters for Describing pH-Dependent Changes in the Adsorption Height of Water Molecules from the $O_B$ and $O_T$ Atomic Planes at the Alumina (012)−Water Interface[a,b]**

| water layers | $pH_t$ | $\Delta z_{low}$ | $\Delta z_{high}$ |
|---|---|---|---|
| $W_{ads1}$ on $O_B$ | 6.5 ± 1.5 | 2.16 ± 0.04 | 1.98 ± 0.03 |
| $W_{ads2}$ on $O_T$ | 10.6 ± 0.8 | 2.23 ± 0.03 | 2.15 ± 0.04 |

[a]$pH_t$: transition pH, $\Delta z_{low}$ and $\Delta z_{high}$: end-member heights of water layers measured from their coordinated surface oxygen groups at extremely low and high pH, i.e., $\Delta z_{1,low}$ ($pH \ll pH_{t1}$) and $\Delta z_{1,high}$ ($pH \gg pH_{t1}$). See Supporting Information Text S4 for details of the model calculation. [b]Fit quality: $\chi^2 = 0.31$ and $R$-factor = 0.9%.

The presence of two transition pH values is qualitatively consistent with earlier SFG studies,[19,20] which reported two characteristic pH values of 4.9 ± 0.4 and 9.2 ± 0.5.[20] Our CTR-derived transition pH values are systematically higher, which we attribute, at least in part, to differences in solution composition and adsorbate identity and coverage between the present work and prior SFG studies.

The observed pH-driven contraction of the interfacial water height with increasing pH and site deprotonation has important implications for changes in the EDL capacitance at the oxide−water interfaces. If the primary hydration layers constitute the inner Helmholtz layer (IHL), the pH-dependent contraction of $W_{ads1}$ toward the surface implies a thinner IHL at higher pH and, all else equal, a larger Helmholtz capacitance. According to a simple parallel-plate picture, the capacitance of an interfacial layer k, $C_k$, is defined as $C_k = \varepsilon_k \varepsilon_0/\beta_k$ where $\varepsilon_k$ and $\beta_k$ are the effective relative permittivity and thickness of layer k and $\varepsilon_0$ is the permittivity of free space. Because interfacial capacitance scales inversely with the effective thickness of this region, this trend is qualitatively consistent with the widely reported increased oxide−electrolyte capacitance below and above the PZNPC, e.g., anatase ($TiO_2$) from 110 to 220 $\mu F/cm^2$,[29] rutile ($TiO_2$) (110) from 63 to 93 $\mu F/cm^2$, and cassiterite ($SnO_2$) from 85 to 130 $\mu F/cm^2$.[30,31]

At the same time, the effective dielectric response $\varepsilon_k$ is sensitive to the interfacial hydrogen-bond network and to field-induced dipole ordering, both of which depend on surface structure and charge density. Thus, $\varepsilon_k$ and $\beta_k$ likely covary with pH; stronger water ordering and dipolar alignment near a more negatively charged surface can both reduce the effective thickness and modify the local permittivity, jointly increasing the Helmholtz capacitance. The pH-dependent contraction of $W_{ads1}$ (Figure 6a), together with the increasing surface deprotonation inferred from our XR and streaming potential data, is therefore consistent with the general trend of increasing interfacial capacitance at more basic pH.

## Changes in the Extended Interfacial Water Structure

Variations in the protonation state alter the polarity and magnitude of the net surface charge, influencing the orientations and sorption geometries of adsorbed water molecules and the organization of the extended interfacial water network at the alumina (012)−water interface. The CTR-derived electron density profiles (Figure 2) show that the extended positional ordering of interfacial water ($W_{ext}$) is strong over the entire pH range investigated. Under neutral and mildly alkaline pH conditions, the water layering is comparably more localized near the surface, reflecting a more confined propagation of surface-induced ordering into the aqueous phase.

This trend in pH-dependent changes of interfacial water structure from CTR analysis is similar to that from previous SFG analyses, which are sensitive to orientational rather than positional ordering of water molecules at the alumina−water interface.[11,19,20] These previous studies reported strong spectroscopic signals from interfacial water molecules in both acidic and basic aqueous solutions. Notably, the signals reversed their sign at the PZNPC (i.e., at pH 6.7), which was interpreted as the reversal in the net polar orientation of

**Table 3. Best-Fit Model Parameters for Describing pH-Dependent Changes in Adsorbed $Rb^+$ Coverage at the Alumina (012)−Water Interface[a]**

| models | $pK_{a1}$ | $pK_{a2}$ | $occ_{tot,0}$ | $occ_{tot,1}$ | $occ_{tot,2}$ |
|---|---|---|---|---|---|
| one-site model[b] | 6.7 ± 1.0 | - | 0.03 ± 0.03 | 0.17 ± 0.06 | - |
| two-site model[c] | 5.3 ± 0.2 | 10.6 ± 0.3 | 0.02 ± 0.01 | 0.14 ± 0.01 | 0.23 ± 0.02 |

[a]$pK_{a1}$ and $pK_{a2}$: primary and secondary equilibrium constants for acid dissociation reactions of the alumina surface, $occ_{tot,0}$: the total $Rb^+$ coverage at pH far below $pK_{a1}$ and $pK_{a2}$, and $occ_{tot,1}$ and $occ_{tot,2}$: increments in $Rb^+$ coverage associated with the negative charge due to the primary and secondary deprotonation reactions, respectively. See Supporting Information Text S5 for details about the model calculation. [b]Fit quality: $\chi^2 = 6.08$ and $R$-factor = 19.7%. [c]Fit quality: $\chi^2 = 0.03$ and $R$-factor = 1.0%.


https://doi.org/10.1021/jacs.5c21453
J. Am. Chem. Soc. 2026, 148, 20399−20411

Downloaded from pubs.acs.org/jacsat/article-pdf/148/20/20399/66197993/jacs.5c21453.pdf by guest on 16 October 2026

the interfacial water molecules. Moreover, the SFG signal was reported to diminish near neutral pH.[11,19,20] This observation was attributed to a decreased spatial extension of oriented water layers at the interface and/or the presence of an equal number of water molecules with opposite orientations relative to the surface, i.e., with their hydrogen atoms pointing either toward or away from the surface functional groups.

## Correlation between $Rb^+$ Uptake and Surface Site Deprotonation

The correlation between $Rb^+$ uptake and surface site deprotonation provides critical insights into the ion adsorption mechanisms driven by electrostatic interactions at the alumina (012)−water interface. The pH-dependent changes in the protonation state of surface functional groups systematically alter the surface charge density, thereby influencing $Rb^+$ adsorption coverage and speciation.

We analyzed the pH-dependent changes in RAXR-derived $Rb^+$ coverage using one-site and two-site models defined with one or two $pK_a$ values, respectively (see Supporting Information Text S5 and Table 3), similar to the analysis carried out for the adsorbed water heights in Figure 6a. The one-site model is the simplest approach to represent the increase in $Rb^+$ coverage as a function of the degree of deprotonation of the alumina surface without molecular distinction between individual surface functional groups. In contrast, the two-site model accounts for the different (de)protonation properties of two functional groups as shown in eqs 1 and 2. This latter model is similar to the one used to analyze changes in the height of adsorbed water layers, as depicted in Figure 6a. Comparing these models provides a means to cross-validate the model structures to express the pH-dependent (de)protonation reactions of the surface functional groups on the alumina surface. We emphasize that the two-site evaluation used here represents an effective, ensemble-averaged description of bridging and terminal aluminol deprotonation. At the microscopic level, the close spacing of $O_B$ and $O_T$ groups can lead to site−site electrostatic coupling and in some cases proton transfer between neighboring oxygens, producing a distribution of local deprotonation free energies. Such correlations can limit the fraction of sites that are simultaneously deprotonated and/or available for strong cation binding at a given pH, providing a plausible explanation for the observed low $Rb^+$ uptake and plateau behavior while the dominant response remains well captured by two effective $pK_a$ values.

At pH 3, both models (Figure 6b) unequivocally show low $Rb^+$ coverages, consistent with the expectation of limited electrostatic attraction of $Rb^+$ to the neutral or positively charged alumina surface in the acidic solutions. The one-site model predicts the pH-dependent increase in $Rb^+$ coverage with a $pK_a$ value of 6.7 ± 1.0 and a maximum coverage of 0.17 ± 0.06 $Rb^+/A_{UC}$ (Table 3). However, this model shows an abrupt increase in $Rb^+$ coverage around the $pK_a$ value, which deviates from the gradual increase in the measured $Rb^+$ coverage across a wider pH range. In comparison, the two-site model provides a better representation of the distribution with a $pK_{a1}$ value of 5.3 ± 0.2 above which the coverage increases up to a plateau value of 0.14 ± 0.01 $Rb^+/A_{UC}$ at pH between 6.5 and 9, and a $pK_{a2}$ value of 10.6 ± 0.3 above which the coverage reaches its maximum value at 0.23 ± 0.02 $Rb^+/A_{UC}$.

The important observation from this model analysis is that the $Rb^+$ adsorption behavior follows the two-$pK_a$ functional shape, consistent with expectation from the classical theory as shown in eqs 1 and 2. That is, the pH-dependent increase in $Rb^+$ coverage results from the increase in negative surface charge due to the deprotonation of the two surface functional groups on the alumina surface. The $pK_a$ values derived from the best-fit two-site model match the $pH_t$ values for expressing the pH-dependent changes in adsorbed water height, within the estimated uncertainties. This agreement indicates strong correlation between the variations in adsorbed $Rb^+$ coverage and changes in adsorbed water height.

Finally, the two-site description in Figure 6b captures the pH-dependent $Rb^+$ uptake using mass-action equilibria tied to site deprotonation without invoking an explicit electrostatic term (e.g., for describing the diffuse layer). This differs from common surface-complexation treatments for oxide powders that include a capacitance-based electrostatic work term.[12] For well-defined single-crystal interfaces, however, several studies have shown that interfacial acid−base and adsorption equilibria can be treated as solution-like reactions without an added electrostatic term, including prior work on the r-cut sapphire/water interface using SFG[11] and recent work on silica.[32] The consistency between the RAXR-derived $Rb^+$ uptake and the CTR-resolved water-layer transitions, together with the limited $Rb^+$ coverage and the pH-dependent contraction of the Stern-layer profile, supports a coherent mechanistic picture. Specifically, it suggests that site-specific interactions and local hydration structure dominate the energetics of $Rb^+$ uptake. Longer-range electrostatic screening is effectively accounted for through the pH-dependent deprotonation of the surface functional groups.

## Surface Charge Compensation and $Rb^+$ Adsorption Structure

The RAXR results show that $Rb^+$ adsorption in the Stern layer increases with pH but that the overall Stern-layer coverage remains modest. The increased $Rb^+$ coverage around the $pK_{a1}$ value, 0.14−0.02 = 0.12 ± 0.01 $Rb^+/A_{UC}$, mainly compensates the surface charge originating from the deprotonated $O_B$ atoms (eq 1). Likewise, the increased $Rb^+$ coverage around the $pK_{a2}$ value, 0.23−0.14 = 0.09 ± 0.02 $Rb^+/A_{UC}$, compensates the surface charge originating from the deprotonated $O_T$ atoms. Considering that there are two $O_B$ and two $O_T$ per $A_{UC}$ of alumina (012), the measured $Rb^+$ coverage corresponds to a small fraction (∼5%) of the surface oxygen sites.

Two factors likely contribute to the observed low Stern-layer $Rb^+$ coverage. First, a non-negligible fraction of charge compensation may occur through a more spatially extended (diffuse) ion distribution. Our RAXR data primarily constrain the ordered, near-surface $Rb^+$ adsorbates and have limited sensitivity to a weak, extended diffuse $Rb^+$ profile. Therefore, the modest Stern-layer coverage quantified by RAXR does not imply that charge compensation occurs exclusively in the Stern layer. Consistent with this interpretation, streaming potential measurements show a negative zeta potential over most of the pH range, confirming that charge compensation extends beyond the ordered Stern-layer $Rb^+$. However, our calculation based on Gouy−Chapman theory[34] indicates that the charge residing above the shear plane is small, implying that this contribution is minor relative to Stern-layer charge compensation (see next section for details).

Downloaded from pubs.acs.org/jacsat/article-pdf/148/20/20399/66197993/jacs.5c21453.pdf by guest on 16 October 2026


https://doi.org/10.1021/jacs.5c21453
J. Am. Chem. Soc. 2026, 148, 20399−20411

Second, local site−site interactions on alumina (012) can limit the number of strongly deprotonated configurations that are simultaneously available for cation binding. On this surface, neighboring $O_B$ and $O_T$ atoms are separated by as little as ∼3 Å, well below the Bjerrum length in water of 7.1 Å, i.e., the distance beyond which electrostatic interaction between two elementary charges becomes negligible.[33] As a result, there is a significant electrostatic penalty for forming adjacent negatively charged sites, which can shift the effective acidity of a site depending on the protonation state of its neighbors. This coupling can broaden the apparent deprotonation behavior and reduce the density of locally favorable binding environments for $Rb^+$, even when the average surface charge becomes increasingly negative with pH. Consistent with this picture, our AIMD trajectories for the negatively charged surface show proton rearrangement between adjacent $O_T$ and $O_B$ groups, suggesting that strictly independent two-site acid−base behavior (eqs 1 and 2) is an effective approximation rather than a complete microscopic description.

In addition to these two effects, the local charge heterogeneity on alumina (012) can influence the adsorption geometry and height distribution of $Rb^+$. Even at high pH, a significant fraction of $O_T$ groups can remain positively charged (eq 2). These positively charged sites can locally hinder close cation approach and contribute to a broader distribution of adsorption heights, because short-range electrostatic repulsion competes with the attraction to nearby deprotonated sites. This provides a plausible explanation for the relatively broad $Rb^+$ adsorption profiles observed by RAXR at intermediate pH values, as well as the progressive contraction of the Stern-layer $Rb^+$ distribution as pH increases, supported by the RAXR and AIMD findings, indicating that more favorable binding environments develop.

## Comparison of XR with AIMD and Zeta Potential Measurements

We relate pH-driven changes in interfacial hydration from CTR and adsorbed $Rb^+$ profiles from RAXR to AIMD predictions and zeta potentials derived from streaming potential measurements to map EDL evolution with pH at the alumina (012)−water interface. It is important to emphasize that each applied technique here probes a different aspect of the interface, making their combination particularly powerful. As such, we focus on pH-dependent trends in the magnitude and spatial distribution of interfacial charge and ion density rather than absolute values. Any quantitative differences are examined in terms of differences in technical sensitivity, probed length scales, and the applied experimental conditions and the simulated systems.

The AIMD simulation predicts IS $Rb^+$ adsorption on both neutral and negatively charged alumina (012) surfaces, with distinct geometries. On the neutral surface, IS $Rb^+$ coordinates primarily with two $O_T$ atoms, with an average adsorption height of 4.3 Å. On the negatively charged surface, IS $Rb^+$ occupies a more strongly surface-coordinated environment, binding to four $O_T$ and two $O_B$ atoms at a significantly shorter average adsorption height of 2.9 Å. The decrease in adsorption height with increasing surface deprotonation is consistent with the RAXR trend observed at higher pH (Table 1).

Beyond the agreement in overall trends, the AIMD height of 2.9 Å for IS $Rb^+$ is comparable to the RAXR-derived values at pH 10.5 and 12 (2.86 ± 0.05 Å and 2.65 ± 0.03 Å, respectively; Table 1). In contrast, the AIMD height for a neutral surface (4.3 Å) exceeds the RAXR values at pH 7 and 8.5 (3.45 ± 0.06 Å and 3.24 ± 0.05 Å, respectively; Table 1). Under neutral to mildly alkaline conditions, the RAXR-derived $Rb^+$ profiles exhibit substantial height distribution widths (Figure 3b) that may include the IS species as well as OS $Rb^+$ ions seen in AIMD (Figure 4). A further one-to-one comparison is complicated by differences in solution composition between the experiments and simulations, as previously discussed. In addition, zeta potential data showed that the interface had a net negative charge in the pH range, which was not reflected in the AIMD calculations.

Comparison of RAXR-inferred Stern layer charge with electrokinetic zeta potentials indicates a consistent picture for the polarity and pH evolution of the interfacial charge. Element-specific RAXR resolves increasing $Rb^+$ uptake with pH and a concomitant decrease in average adsorption height, both signatures of an increasingly negative surface due to deprotonation of $>Al_3O$ and >AlO sites. The zeta potentials are negative over the entire pH range and become more negative with increasing pH, also consistent with progressive surface deprotonation.

A semiquantitative reconciliation of magnitudes is also plausible when considering the different regions of EDL that each technique integrates. At pH 5−8.5, the RAXR-inferred Stern charge increases from +0.04 to +0.10 $C/m^2$ while zeta potentials become progressively more negative. Both trends reflect the increasing deprotonation on $>Al_3O$ (followed by >AlO), as independently inferred from the CTR-derived water-layer height transitions. At pH ≥ 7 for a 1:1 electrolyte at 10 mM, a zeta potential of around −40 mV corresponds to an electrokinetic charge density at the shear plane ($\sigma_s$) of approximately −0.01 $C/m^2$, calculated based on the Gouy−Chapman theory[34] as

$$\sigma_s = 0.1174 I^{1/2} \sinh[c\zeta F/(2RT)] \quad (3)$$

where $I$ is the ionic strength, $c$ is the ion charge, $\zeta$ is the zeta potential, and $F$ is the Faraday constant (96,485 C/mol). This calculated value is significantly smaller than the surface charge compensated by the RAXR-derived Stern-layer $Rb^+$ at pH 12 (+0.15 $C/m^2$; Table 1). Assuming that the shear plane is located between the Stern layer and diffuse layer, this difference implies that most of the negative surface charge is compensated within the Stern layer, with a minor residual charge carried into the diffuse layer. Together, these steps would enable a more rigorous, cross-validated partitioning of charge between Stern and diffuse layers and sharpen the mechanistic link between local adsorption structure and macroscopic electrokinetics.

Direct, quantitative comparison nevertheless faces several limitations. First, zeta potential reflects the potential at the hydrodynamic shear plane, the location of which relative to the outer Helmholtz plane is not known *a priori* and may change with pH, ionic strength, and adsorbate ions, which can alter the integrity of interfacial hydration structure. In contrast, the RAXR data in our study may lack sensitivity to the diffuse profile ions and does not capture any anion adsorption or contributions from hydroxide and hydronium ions. Conversely, zeta potential arises from the surface charge and the surrounding ion atmosphere of the EDL and is related to, but not equal to, the net proton-related charge carried with the substrate. Finally, zeta potential data analysis depends on electrokinetic modeling based on assumptions on various physical factors, e.g., interfacial viscosity and channel geometry,

Downloaded from pubs.acs.org/jacsat/article-pdf/148/20/20399/66197993/jacs.5c21453.pdf by guest on 16 October 2026


https://doi.org/10.1021/jacs.5c21453
J. Am. Chem. Soc. 2026, 148, 20399−20411

with limited consideration on variabilities in structure and chemistry resulting from surface preparation and site-specific reaction processes as highlighted from AIMD simulations and RAXR analysis.

## ■ CONCLUSIONS

The results provide a molecular-scale description of how site-specific deprotonation on alumina (012) controls interfacial water structure and $Rb^+$ adsorption. Changes in the water structure are subtle but systematic, with adsorption heights shifting around two transition pH values, $pH_{t,1}(>Al_3O) = 6.5 \pm 1.5$ and $pH_{t,2}(>AlO) = 10.6 \pm 0.8$. A two-site model captures the similar pH-dependent increase in adsorbed $Rb^+$ coverage, yielding $pK_{a1}(>Al_3O) = 5.3 \pm 0.2$ and $pK_{a2}(>AlO) = 10.6 \pm 0.3$. The close correspondence between these $pH_t$ and $pK_a$ values, and their agreement with accepted ranges, supports a self-consistent picture in which deprotonation of bridging and terminal aluminol groups drives the progressive development of negative surface charge.

Despite the increasing surface charge at high pH, the maximum Stern-layer $Rb^+$ coverage remains modest. This limited uptake, combined with the RAXR- and AIMD-derived contraction of the Stern layer and the persistently negative zeta potentials, indicates that charge compensation is shared between specifically adsorbed counterions and a residual diffuse-layer contribution, and that local electrostatic interactions among neighboring surface sites strongly modulate deprotonation and ion binding. Beyond confirming pH sensitivity, our results provide direct, quantitative structure−chemistry relationships: distinct aluminol (de)protonation events produce discrete hydration-layer reorganizations and measurable changes in Stern-layer ion binding distances. This resolves a long-standing gap between macroscopic electrokinetic trends and molecular-scale EDL structure at oxide−water interfaces.

By explicitly linking surface protonation state, hydration-layer geometry, and adsorbed-ion speciation, this work establishes quantitative benchmarks for next-generation surface-complexation and reactive-transport models of oxide−water interfaces. The demonstrated coupling between surface protonation, hydration-layer evolution, and adsorbed-ion speciation suggests practical routes to adjust electrostatic screening and ion selectivity at oxide interfaces relevant to ion separation, corrosion mitigation, and heterogeneous catalysis. More broadly, the combined experimental and computational works presented here provide a transferable framework for interrogating and ultimately engineering EDLs at a wide range of metal oxide−water and electrode−electrolyte interfaces.

## ■ ASSOCIATED CONTENT

### Data Availability Statement

The data underlying this study are openly available at https://www.doi.org/10.17038/CSE/3025395.

### Supporting Information

The Supporting Information is available free of charge at https://pubs.acs.org/doi/10.1021/jacs.5c21453.

AIMD-Atom-Coordinates-Alumina012-Rb-Negatively-Charged-Surface.pdb (PDB)

AIMD-Atom-Coordinates-Alumina012-Rb-Neutral-Surface.pdb (PDB)

AIMD-Atom-Coordinates-Alumina012-Rb-Positively-Charged-Surface.pdb (PDB)

Materials and methods; CTR and RAXR data analysis procedure; determination of the point of zero charge on alumina surfaces; adsorbed water height analysis; adsorbed $Rb^+$ coverage analysis; alumina crystal structure and (012) termination; calculation of the surface potential of alumina (012); atomic force microscopy images of alumina (012); schematic of synchrotron XR measurements; complete in situ CTR and normalized CTR data of the alumina (012)−water interfaces; complete Rb RAXR spectra; atomic displacements at the alumina (012)−water interface; best-fit model parameters for CTR data; and comparison of the quality of fits for CTR analysis (PDF)

## ■ AUTHOR INFORMATION


### Corresponding Authors

**Julia Neumann** − *Chemical Sciences and Engineering Division, Argonne National Laboratory, Lemont, Illinois 60439, United States;* orcid.org/0000-0002-3650-3967; Email: jneumann@anl.gov

**Sang Soo Lee** − *Chemical Sciences and Engineering Division, Argonne National Laboratory, Lemont, Illinois 60439, United States;* orcid.org/0000-0001-8585-474X; Email: sslee@anl.gov

### Authors

**YoungJae Kim** − *Chemical Sciences and Engineering Division, Argonne National Laboratory, Lemont, Illinois 60439, United States;* Present Address: Division of Earth and Environmental System Sciences, Major of Environmental Geosciences, Pukyong National University, Busan, Republic of Korea

**Xiaoyu Wang** − *Ralph E. Martin Department of Chemical Engineering, University of Arkansas, Fayetteville, Arkansas 72701, United States;* orcid.org/0000-0003-2228-0114

**Katherine J. Harmon** − *Applied Physics Graduate Program, Northwestern University, Evanston, Illinois 60208, United States;* Present Address: Department of Materials Science and Engineering, Stanford University, Stanford, CA 94305, United States.; orcid.org/0000-0001-6427-7971

**Amanda J. Carr** − *Chemical Sciences and Engineering Division, Argonne National Laboratory, Lemont, Illinois 60439, United States;* orcid.org/0000-0002-8224-7677

**Johannes Lützenkirchen** − *Institute for Nuclear Waste Disposal (INE), Karlsruhe Institute for Technology (KIT), 76344 Eggenstein-Leopoldshafen, Germany;* orcid.org/0000-0002-0611-2746

**Paul Fenter** − *Chemical Sciences and Engineering Division, Argonne National Laboratory, Lemont, Illinois 60439, United States;* orcid.org/0000-0002-6672-9748

Complete contact information is available at: https://pubs.acs.org/10.1021/jacs.5c21453


### Author Contributions

The manuscript was written through contributions of all authors. All authors have given approval to the final version of the manuscript.


### Funding

This work was funded by the U.S. Department of Energy (DOE), Office of Science, Office of Basic Energy Sciences, Geosciences program (FWP 57814) under Contract DE-


Downloaded from pubs.acs.org/jacsat/article-pdf/148/20/20399/66197993/jacs.5c21453.pdf by guest on 16 October 2026

AC02-06CH11357 to UChicago Argonne, LLC as operator of Argonne National Laboratory. Streaming potential measurements and analysis by AJC were supported by Laboratory Directed Research and Development (LDRD) funding from Argonne National Laboratory, provided by the Director, Office of Science, of the U.S. Department of Energy under Contract No. DE-AC02-06CH11357. CTR and RAXR measurements were conducted at Beamline 33-ID-D at the Advanced Photon Source (APS), Argonne National Laboratory. This research used resources of the Advanced Photon Source, a U.S. Department of Energy (DOE) Office of Science User Facility operated for the DOE Office of Science by Argonne National Laboratory under Contract DE-AC02-06CH11357. XW acknowledges the computing resources provided on Improv, a high-performance computing cluster operated by the Laboratory Computing Resource Center at Argonne National Laboratory.

## Notes

The authors declare no competing financial interest.

## ■ REFERENCES

(1) Bañuelos, J. L.; Borguet, E.; Brown, G. E.; Cygan, R. T.; Deyoreo, J. J.; Dove, P. M.; Gaigeot, M. P.; Geiger, F. M.; Gibbs, J. M.; Grassian, V. H.; Ilgen, A. G.; Jun, Y. S.; Kabengi, N.; Katz, L.; Kubicki, J. D.; Lützenkirchen, J.; Putnis, C. V.; Remsing, R. C.; Rosso, K. M.; Rother, G.; Sulpizi, M.; Villalobos, M.; Zhang, H. Oxide- and Silicate-Water Interfaces and Their Roles in Technology and the Environment. *Chem. Rev.* **2023**, *123* (10), 6413−6544.

(2) Brown, G. E.; Henrich, V. E.; Casey, W. H.; Clark, D. L.; Eggleston, C.; Felmy, A.; Goodman, D. W.; Grätzel, M.; Maciel, G.; McCarthy, M. I.; Nealson, K. H.; Sverjensky, D. A.; Toney, M. F.; Zachara, J. M. Metal Oxide Surfaces and Their Interactions with Aqueous Solutions and Microbial Organisms. *Chem. Rev.* **1999**, *99* (1), 77−174.

(3) Catalano, J. G.; Trainor, T. P.; Eng, P. J.; Waychunas, G. A.; Brown, G. E. CTR Diffraction and Grazing-Incidence EXAFS Study of U(VI) Adsorption onto $\alpha$-$Al_2O_3$ and $\alpha$-$Fe_2O_3$ (1−102) Surfaces. *Geochim. Cosmochim. Acta* **2005**, *69* (14), 3555−3572.

(4) Kupcik, T.; Rabung, T.; Lützenkirchen, J.; Finck, N.; Geckeis, H.; Fanghänel, T. Macroscopic and Spectroscopic Investigations on Eu(III) and Cm(III) Sorption onto Bayerite ($\beta$-$Al(OH)_3$) and Corundum ($\alpha$-$Al_2O_3$). *J. Colloid Interface Sci.* **2016**, *461*, 215−224.

(5) Neumann, J.; Carr, A. J.; Lessing, J.; Soderholm, L.; Catalano, J. G.; Fenter, P.; Lee, S. S. Unraveling pH-Dependent Changes in Adsorption Structure of Uranyl on Alumina (012). *J. Phys. Chem. Lett.* **2024**, *15* (13), 3493−3501.

(6) Fang, Y.; Lee, S. S.; Ledingham, G. J.; Stubbs, J. E.; Eng, P. J.; Catalano, J. G. Complex Adsorption Behavior of Neodymium and Ytterbium on Structurally-Distinct Alumina Surfaces. *Environ. Sci. Technol.* **2025**, *59*, 3972.

(7) Catalano, J. G. Weak Interfacial Water Ordering on Isostructural Hematite and Corundum (001) Surfaces. *Geochim. Cosmochim. Acta* **2011**, *75* (8), 2062−2071.

(8) Catalano, J. G. Relaxations and Interfacial Water Ordering at the Corundum (110) Surface. *J. Phys. Chem. C* **2010**, *114* (14), 6624−6630.

(9) Catalano, J. G.; Park, C.; Zhang, Z.; Fenter, P. Termination and Water Adsorption at the $\alpha$-$Al_2O_3$ (012)-Aqueous Solution Interface. *Langmuir* **2006**, *22* (10), 4668−4673.

(10) Xu, T.; Stubbs, J. E.; Eng, P. J.; Catalano, J. G. Comparative Response of Interfacial Water Structure to pH Variations and Arsenate Adsorption on Corundum (0 1 2) and (0 0 1) Surfaces. *Geochim. Cosmochim. Acta* **2019**, *246*, 406−418.

(11) Sung, J.; Zhang, L.; Tian, C.; Shen, Y. R.; Waychunas, G. A. Effect of pH on the Water/$\alpha$-$Al_2O_3$ (1−102) Interface Structure Studied by Sum-Frequency Vibrational Spectroscopy. *J. Phys. Chem. C* **2011**, *115* (28), 13887−13893.

(12) Hiemstra, T.; Yong, H.; Van Riemsdijk, W. H. Interfacial Charging Phenomena of Aluminum (Hydr)Oxides. *Langmuir* **1999**, *15* (18), 5942−5955.

(13) Franks, G. V.; Meagher, L. The Isoelectric Points of Sapphire Crystals and Alpha-Alumina Powder. *Colloids Surf. A Physicochem. Eng. Asp.* **2003**, *214* (1−3), 99−110.

(14) Lützenkirchen, J. Specific Ion Effects at Two Single-Crystal Planes of Sapphire. *Langmuir* **2013**, *29* (25), 7726−7734.

(15) Fitts, J. P.; Shang, X.; Flynn, G. W.; Heinz, T. F.; Eisenthal, K. B. Electrostatic Surface Charge at Aqueous/$\alpha$-$Al_2O_3$ Single-Crystal Interfaces as Probed by Optical Second-Harmonic Generation. *J. Phys. Chem. B* **2005**, *109* (16), 7981−7986.

(16) Kershner, R. J.; Bullard, J. W.; Cima, M. J. Zeta Potential Orientation Dependence of Sapphire Substrates. *Langmuir* **2004**, *20* (10), 4101−4108.

(17) Wang, Y.; Persson, P.; Michel, F. M.; Brown, G. E., Jr Comparison of Isoelectric Points of Single-Crystal and Polycrystalline $\alpha$-$Al_2O_3$ and $\alpha$-$Fe_2O_3$ Surfaces. *Am. Mineral.* **2016**, *101* (10), 2248−2259.

(18) Wang, Z.; Lee, S. W.; Catalano, J. G.; Lezama-Pacheco, J. S.; Bargar, J. R.; Tebo, B. M.; Giammar, D. E. Adsorption of Uranium(VI) to Manganese Oxides: X-Ray Absorption Spectroscopy and Surface Complexation Modeling. *Environ. Sci. Technol.* **2013**, *47* (2), 850−858.

(19) Sung, J.; Zhang, L.; Tian, C.; Waychunas, G. A.; Shen, Y. R. Surface Structure of Protonated r-Sapphire (1−102) Studied by Sum-Frequency Vibrational Spectroscopy. *J. Am. Chem. Soc.* **2011**, *133* (11), 3846−3853.

(20) Sung, J.; Shen, Y. R.; Waychunas, G. A. The Interfacial Structure of Water/Protonated $\alpha$-$Al_2O_3$ (1−102) as a Function of pH. *J. Phys.: Condens. Matter* **2012**, *24* (12), 124101.

(21) Stumm, W. *Chemistry of the Solid-Water Interface: Processes at the Mineral-Water and Particle-Water Interface in Natural Systems*; John Wiley & Son Inc.: New York, 1992.

(22) Trainor, T. P.; Eng, P. J.; Brown, G. E.; Robinson, I. K.; Santis, M. D.; Brown, G. E., Jr; Robinson, I. K.; De Santis, M. Crystal Truncation Rod Diffraction Study of the $\alpha$-$Al_2O_3$ (1−102) Surface. *Surf. Sci.* **2002**, *496* (3), 238−250.

(23) Fulton, J. L.; Pfund, D. M.; Wallen, S. L.; Newville, M.; Stern, E. A.; Ma, Y. Rubidium Ion Hydration in Ambient and Supercritical Water. *J. Chem. Phys.* **1996**, *105* (6), 2161−2166.

(24) Lessing, J.; Neumann, J.; Lützenkirchen, J.; Bok, F.; Moisei-Rabung, S.; Schild, D.; Brendler, V.; Stumpf, T.; Schmidt, M. Natural and Synthetic Plagioclases: Surface Charge Characterization and Sorption of Trivalent Lanthanides (Eu) and Actinides (Am, Cm). *Colloids Surf. A Physicochem. Eng. Asp.* **2024**, *688* (February), 133529.

(25) Trainor, T. P.; Templeton, A. S.; Brown, G. E.; Parks, G. A. Application of the Long-Period X-ray Standing Wave Technique to the Analysis of Surface Reactivity: Pb(II) Sorption at $\alpha$-$Al_2O_3$/Aqueous Solution Interfaces in the Presence and Absence of Se(VI). *Langmuir* **2002**, *18* (15), 5782−5791.

(26) Zhang, Z.; Fenter, P.; Sturchio, N. C.; Bedzyk, M. J.; Machesky, M. L.; Wesolowski, D. J. Structure of Rutile $TiO_2$ (110) in Water and 1 Molal $Rb^+$ at pH 12: Inter-Relationship among Surface Charge, Interfacial Hydration Structure, and Substrate Structural Displacements. *Surf. Sci.* **2007**, *601* (4), 1129−1143.

(27) Tanwar, K. S.; Lo, C. S.; Eng, P. J.; Catalano, J. G.; Walko, D. A.; Brown, G. E.; Waychunas, G. A.; Chaka, A. M.; Trainor, T. P. Surface Diffraction Study of the Hydrated Hematite (1−102) Surface. *Surf. Sci.* **2007**, *601* (2), 460−474.

(28) Catalano, J. G.; Fenter, P.; Park, C. Interfacial Water Structure on the (012) Surface of Hematite: Ordering and Reactivity in Comparison with Corundum. *Geochim. Cosmochim. Acta* **2007**, *71* (22), 5313−5324.

(29) Schindler, P. W.; Gamsjäger, H. Acid—Base Reactions of the $TiO_2$ (Anatase)—Water Interface and the Point of Zero Charge of $TiO_2$ Suspensions. *Kolloid Z. Z. Polym.* **1972**, *250* (7), 759−763.

Downloaded from pubs.acs.org/jacsat/article-pdf/148/20/20399/66197993/jacs.5c21453.pdf by guest on 16 October 2026

(30) Zhang, C.; Hutter, J.; Sprik, M. Coupling of Surface Chemistry and Electric Double Layer at $TiO_2$ Electrochemical Interfaces. *J. Phys. Chem. Lett.* **2019**, *10* (14), 3871−3876.
(31) Jia, M.; Zhang, C.; Cheng, J. Origin of Asymmetric Electric Double Layers at Electrified Oxide/Electrolyte Interfaces. *J. Phys. Chem. Lett.* **2021**, *12* (19), 4616−4622.
(32) Li, X.; Brigiano, F. S.; Pezzotti, S.; Liu, X.; Chen, W.; Chen, H.; Li, Y.; Li, H.; Lin, X.; Zheng, W.; et al. Unconventional Structural Evolution of an Oxide Surface in Water Unveiled by in Situ Sum-Frequency Spectroscopy. *Nat. Chem.* **2025**, *17* (2), 198−203.
(33) Levin, Y. Electrostatic Correlations: From Plasma to Biology. *Rep. Prog. Phys.* **2002**, *65* (11), 1577−1632.
(34) Langmuir, D. *Aqueous Environmental Geochemistry*: New Jersey, 1997.
(35) Lee, S. S.; Fenter, P.; Nagy, K. L.; Sturchio, N. C. Monovalent Ion Adsorption at the Muscovite (001) − Water Interface: Relationships among Ion Coverage and Speciation, Interfacial Water Structure, and Substrate Relaxation. *Langmuir* **2012**, *28*, 8637−8650.
(36) Lee, S. S.; Fenter, P.; Nagy, K. L.; Sturchio, N. C. Real-time Observation of Cation Exchange Kinetics and Dynamics at the Muscovite-Water Interface. *Nat. Commun.* **2017**, *8*, 15826.

Downloaded from pubs.acs.org/jacsat/article-pdf/148/20/20399/66197993/jacs.5c21453.pdf by guest on 16 October 2026



https://doi.org/10.1021/jacs.5c21453
*J. Am. Chem. Soc.* 2026, 148, 20399−20411